

# Journal of Geophysical Research: Oceans

## RESEARCH ARTICLE

10.1002/2014JC009810

**Key Points:**

- Different methods for detecting ACC jets reveal differing jet structures
- Methods from signal processing can improve jet detection techniques
- Some methods fail in the presence of strong eddy fields

**Correspondence to:**

C. C. Chapman,  
chris.chapman.28@gmail.com

**Citation:**

Chapman, C. C. (2014), Southern Ocean jets and how to find them: Improving and comparing common jet detection methods, *J. Geophys. Res. Oceans*, 119, 4318–4339, doi:10.1002/2014JC009810.

Received 10 JAN 2014

Accepted 21 JUN 2014

Accepted article online 26 JUN 2014

Published online 16 JUL 2014

## Southern Ocean jets and how to find them: Improving and comparing common jet detection methods

**Christopher C. Chapman<sup>1,2</sup>**

<sup>1</sup>Research School of Earth Sciences and ARC Centre of Excellence for Climate System Science, Australian National University, Canberra, ACT, Australia, <sup>2</sup>CSIRO Wealth From Oceans Flagship, Hobart, Tasmania, Australia

**Abstract** This study undertakes a detailed comparison of different methods used for detecting and tracking oceanic jets in the Southern Ocean. The methods under consideration are the gradient thresholding method, the probability density function (PDF) method, and the contour method. Some weaknesses of the gradient thresholding method are discussed and an enhancement (the WHOSE method), based on techniques from signal processing, is proposed. The WHOSE method is then compared to the other three methods. Quantitative comparison is undertaken using synthetic sea-surface height fields. The WHOSE method and the contour method are found to perform well even in the presence of a strong eddy field. In contrast, the standard gradient thresholding and PDF methods only perform well in high signal-to-noise ratio situations. The WHOSE, PDF, and the contour methods are then applied to data from the eddy-resolving Ocean General Circulation Model for the Earth Simulator. While the three methods are in broad agreement on the location of the main ACC jets, the nature of the jet fields they produce differ. In particular, the WHOSE method reveals a fine-scale jet field with complex braiding behavior. It is argued that this fine-scale jet field may affect the calculation of eddy diffusivities. Finally, recommendations based on this study are made. The WHOSE and gradient thresholding methods are more suitable for the study of jets as localized strong currents, useful for studies of tracer fluxes. The contour and PDF methods are recommended for studies linking jets to hydrographic fronts.

### 1. Introduction

Jets are ubiquitous in geophysical fluid dynamics. They are the dominant dynamical feature of the Southern Ocean and the Antarctic Circumpolar Current (ACC) [Thompson, 2008; Ivchenko et al., 2013], the midlatitude atmosphere [Dritschel and McIntyre, 2008], and the atmospheres of giant planets [Kaspi and Flierl, 2007]. Despite their frequent presence in fluid dynamics, it is difficult to give a precise definition of a jet [Rhines, 1994]. Jets are generally long but relatively thin and have an anisotropic velocity field, with one dominant flow direction. The lack of a precise definition of jets has led to difficulties in their identification. The detection of jets in the ocean, where the cross-jet spatial scale is of similar order to the scale of mesoscale eddies, is particularly difficult [Thompson, 2008].

Our ability to detect oceanic jets has greatly influenced our understanding of the dynamics of regions where they are present. In the Southern Ocean, the work of Orsi et al. [1995] and Belkin and Gordon [1996] exploited the fact that jets are related to hydrographic “fronts.” There is some confusion in the literature about the terms “front” and “jet,” with the two often being used interchangeably. This confusion is discussed in detail in Graham and De Boer [2013]. In this paper, a “jet” is a strong current, while a “front” is a water mass boundary. These boundaries occur as jets tend to act as mixing barriers and reduce cross-frontal exchange of tracers [Dritschel and McIntyre, 2008; Ferrari and Nikurashin, 2010; Klocker et al., 2012]. Thus, hydrographic quantities that denote different water masses (such as salinity or dissolved oxygen) undergo rapid changes across jet cores. Using this effect and historical hydrographic data, both Orsi et al. [1995] and Belkin and Gordon [1996] developed maps of Southern Ocean front positions. The conceptual model of the Southern Ocean produced in these papers has become known as the “traditional” view of the ACC [Sokolov and Rintoul, 2007; Langlais et al., 2011]: three circumpolar fronts that were relatively time invariant and coherent over the entire circumpolar range.

With the availability of high-quality satellite data sets and advances in numerical modeling, an alternative view of jets in the Southern Ocean has emerged: that ACC jets are strong geostrophic currents that

meander, strengthen, weaken, split, and merge [Gille, 1994; Hughes and Ash, 2001; Sokolov and Rintoul, 2007; Sallée *et al.*, 2008; Sokolov and Rintoul, 2009a]. These currents are coincident with strong sea-surface height (SSH) and/or sea-surface temperature (SST) gradients. Exploiting this fact, a number of studies have used SSH or SST gradients to determine the locations of jets [Moore *et al.*, 1999; Hughes and Ash, 2001; Kostianoy *et al.*, 2004; Burls and Reason, 2006; Dong *et al.*, 2006; Graham *et al.*, 2012; De Boer *et al.*, 2013; Graham and De Boer, 2013]. A jet is detected when the gradient exceeds some predefined threshold. The physical interpretation of this thresholding operation is simply: how strong must the geostrophic current be to be considered a jet? If the value of the threshold is too high, valid currents are rejected; too low and the method reports false positives. Gradient thresholding methods yield time mean jet positions that are generally close to the accepted hydrographic front positions, but show substantial time variability [Graham *et al.*, 2012].

Gradient thresholding relies on taking derivatives of fields. Differentiation both reduces the effective resolution of the field and amplifies noise, which can result in large errors, both in the magnitude and location of the jet. These methods also struggle to distinguish between jets and mesoscale eddies. Sokolov and Rintoul [2002, 2007], in an attempt to reconcile the “traditional” view of the Southern Ocean from hydrography and the more dynamic view from satellite data, introduced a set of methods that have come to be known as “contour methods,” that reduce the impact of eddies on jet locations. The primary insight made by Sokolov and Rintoul [2002] was that regions of strong SSH gradients, typical of a jet, are often associated with a unique value of the SSH. As such, the location of a that SSH contour marks the location of the jet. In general, the contour method requires:

1. Regions of high  $|\nabla \text{SSH}|$  to be identified.
2. A fitting procedure used to determine the value of SSH that represents each contiguous high  $|\nabla \text{SSH}|$  region.

Methods based on this approach have been used by a number of authors to provide evidence of spatial and temporal frontal variability [Sokolov and Rintoul, 2009b, 2009a; Billany *et al.*, 2010; Volkov and Zlotnicki, 2012], yielding maps of as many as 10 continuous, circumpolar jets. These studies differ in the fitting procedure used to determine the SSH contour to associate with particular jets. Sokolov and Rintoul [2007] used an optimization routine designed to choose SSH contours so that as much of the Southern Ocean area with high  $|\nabla \text{SSH}|$  was accounted for as possible. Volkov and Zlotnicki [2012] used a simpler method: integrating  $|\nabla \text{SSH}|$  along SSH contours allowed them to determine which SSH contours were associated with jets.

Despite a simpler methodology, Volkov and Zlotnicki's [2012] analysis gives similar results to Sokolov and Rintoul [2007]. Sallée *et al.* [2008] and Langlais *et al.* [2011] used a hybrid of hydrological and dynamical methods, fitting transport maxima to carefully selected isotherms, to give a picture of Southern Ocean jets similar to that of Sokolov and Rintoul [2007]: up to five dynamic circumpolar jets, that meander, split, and merge.

Graham *et al.* [2012] have cast doubt on the global applicability of contour-type methods. Frequently, a SSH value associated with a particular jet would be found in regions with no enhanced SSH gradient. In addition, they noted that the SSH value associated with a particular region of enhanced SSH gradient can change in both time and space, concluding that variability of a particular SSH contour does not always imply variability of the jet. This criticism is supported by Thompson *et al.* [2010] and Thompson and Sallée [2012] who used probability density functions (PDFs) of potential vorticity (PV) in an eddy-resolving model to show that the PV value associated with a particular jet can change, both spatially and temporally. Langlais *et al.* [2011] noted that narrow SSH gradients are in fact broad in SSH space. When jets are weak, a small error in SSH can result in a disproportionately large error in the location of the jet. The net effect of these disadvantages is that contour methods, although a vital tool for the study of the ACC, must be used with care and possibly in conjunction with other methods to confirm jet locations.

As mentioned above, Thompson *et al.* [2010] introduced PDFs to the detection of oceanographic jets, although this method had previously been used to demonstrate the mixing of PV in the ACC [Marshall *et al.*, 1993]. To explain the method, consider a jet that manifests as a sharp gradient in a particular geophysical field (for example, SSH) flanked by regions where that field is homogenized, a situation common in geophysical fluids [Dritschel and McIntyre, 2008]. A histogram of SSH values taken across the jet would find the frequency of SSH values in the homogenized regions to be high, and the frequency of SSH values in the

gradient regions to be low. Thus, high gradient regions manifest as PDF minima. Using the PDFs, jets can be detected in two ways:

1. The PDF can be mapped to spatial coordinates. Local minima in the spatially mapped PDF correspond to the location of jets; or
2. The values of SSH at the PDF minima can be determined. Jets are taken to be associated with these values in a similar manner to contour methods. The values of the SSH or PV can then be tracked in time and space to give the location of the jet.

PDF methods avoid several of the problems associated with contour methods. PDF methods allow for a local definition of the SSH/PV contour value that can evolve in time and space, as well as easily identifying regions of homogenized SSH or PV along a jet's path, is useful for assessing locations of enhanced mixing [Thompson *et al.*, 2010].

### 1.1. Interpreting the Results of Different Jet Detection Methods

The methods of Sokolov and Rintoul [2007], Thompson *et al.* [2010], and Langlais *et al.* [2011] are suited to global or large domain studies: PDF methods rely on the collection of a large enough number of points to construct meaningful PDFs, while the contour methods involve fitting SSH gradients to either SSH or temperature contours over large regions. The advantage of these methods is that they are able to link strong jets to hydrographic quantities, somewhat reconciling the "traditional" view of the ACC from hydrography and the "dynamic" view from remote sensing. Additionally, these methods are able to link together jets in different geographical locations by noting that a particular SSH contour will (generally) retain certain water mass properties as it varies in space and time, although the strength of this relationship recently become a matter of debate [Graham and De Boer, 2013]. Linking together different geographic regions in this way allows features separated by large distances to be viewed as the manifestations of the same physical object: an ACC front. These global methods also allow the flux of water mass properties from one region to another to be calculated in a conceptually clear manner.

Despite the circumpolar view of fronts offered by contour-type methods, the high SSH gradients that define dynamical jets are not necessarily continuous throughout space and time, instead being weak or nonexistent at certain locations or times along a SSH contour. Jets as discontinuous filaments are the view that emerges from the application of gradient thresholding methods to data sets that resolve or permit meso-scale features [Hughes and Ash, 2001; Graham *et al.*, 2012]. Gradient thresholding methods are more suited to the study of jets as local, rather than global features, as all the information required to determine a jet's location is found *locally*. Viewing jets as local features is perhaps more realistic than viewing jets as circumpolar features [Graham *et al.*, 2012], although it is no longer simple to link jets to water masses. Seeing jets as local features is not meant to imply that gradient thresholding is unsuitable studying the global jet field, only that the information used to derive the jet's location is obtained locally. Unlike the contour or PDF methods, gradient thresholding cannot be used, on its own, to link together geographically separated features.

As high-resolution simulations and data sets become more common and are better able to resolve the oceanic mesoscale, whether jets are analyzed as local or global features is likely to become an important question. Additionally, the problem of separating jets from eddies becomes more pronounced. In this study, we:

Introduce a new method to enhance gradient thresholding that reduces the impact of eddies, using techniques taken from signal processing;

Undertake a quantitative comparison of different jet detection methods using synthetic data where the exact position of jets to be determined is known *a priori*;

Undertake a qualitative comparison of different jet detection methods using data from a high-resolution ocean model.

While there are numerous studies that have provided qualitative comparisons of different jet detection methodologies [Thompson *et al.*, 2010; Langlais *et al.*, 2011; Graham *et al.*, 2012] there have been few, if any, attempts to make quantitative comparisons of these methods, partially due to the potential ambiguity of defining jets in data: how can one be sure of the "exact" position of a jet prior to its detection? In this paper, we address this problem by using synthetic data where the position of the jets is set in advance. Knowing

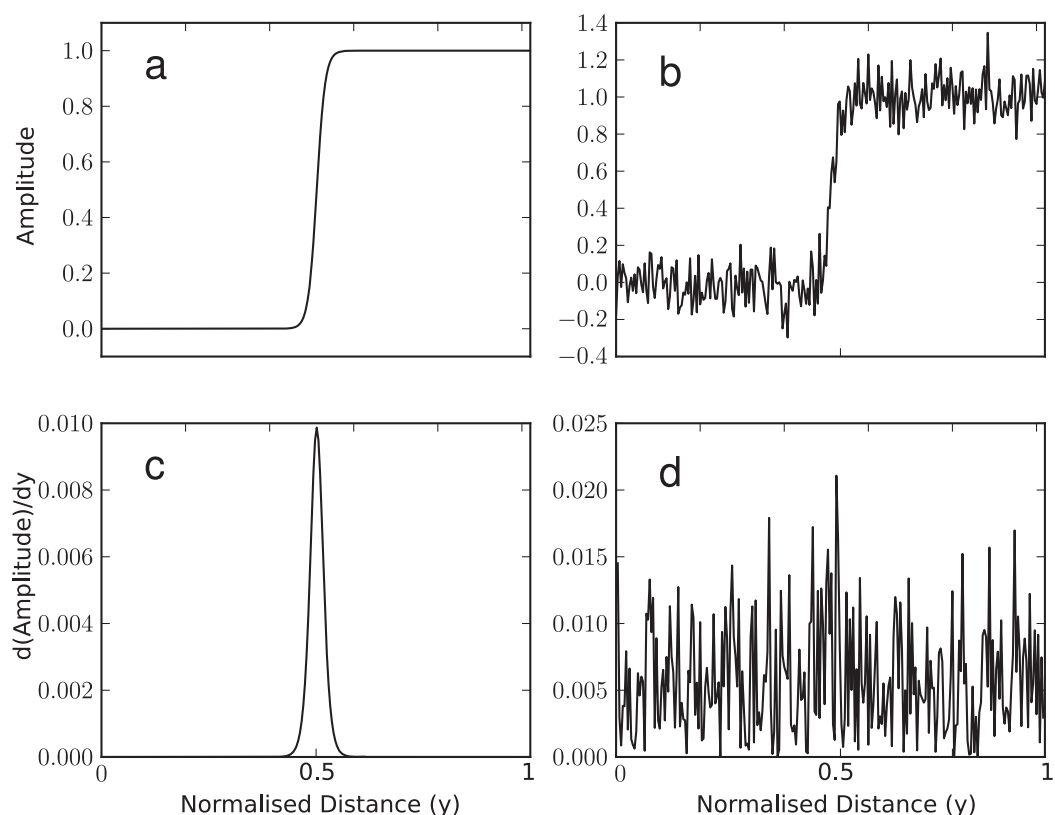


**Figure 1.** (a) An example step signal with a finite rise time; (b) same step signal with the addition of random Gaussian white noise with a signal-to-noise ratio of 20 dB; (c) the gradient of the noiseless signal computed using central differences; (d) the absolute value of the gradient of the noisy signal. Note that the scale of the y axis differs between Figures 1c and 1d, with the noisy signal having gradient magnitudes a factor of  $\sim 2$  larger than the noiseless signal.

the a priori location of jets allows the computation of statistics with the form  $\text{error} = \text{detected position} - \text{true position}$ . Similar methodologies have been employed by Luo and Jameson [2002] in the detection of oceanographic eddies.

In section 2, we discuss several problems with gradient thresholding, present a review of methods for the detection of steps and pulses in signal processing, and show how they can be applied to oceanographic data. In section 3, we compare the accuracy of a number of commonly used jet detection methods using synthetic data designed to resemble the SSH field of the Southern Ocean. In section 4, we demonstrate how the choice of jet detection method affects the jet structure in a high-resolution model of the Southern Ocean. In section 5, we discuss the implications of jet detection methodologies for the study of the ACC.

## 2. Locating Oceanic Jets Using Step Detection Methods

### 2.1. Review of Methods From Signal Processing

In this section, we briefly review the concept of step detection and some methods directly relevant to this paper. This field is mature and the body of associated literature is large. Thus, our review is cursory. Readers seeking more information are directed to the review articles of Carter *et al.* [2008] and Nadernejad *et al.* [2008]. Most step detection methods share a common thread: the step or pulse is associated with localized increase in the signal gradient.

Noise complicates the problem. Even in situations where the signal-to-noise ratio (SNR) is high, computing the gradient can yield many local gradient maxima, which can give false positive results. We illustrate this effect in Figure 1. The gradient of the uncorrected signal (Figures 1a and 1c) shows a strong maximum at the location of the step. However, with the addition of noise (Figures 1b and 1d), the gradient no longer accurately detects the step, despite the step being clearly evident to the eye in Figure 1b. One can attempt

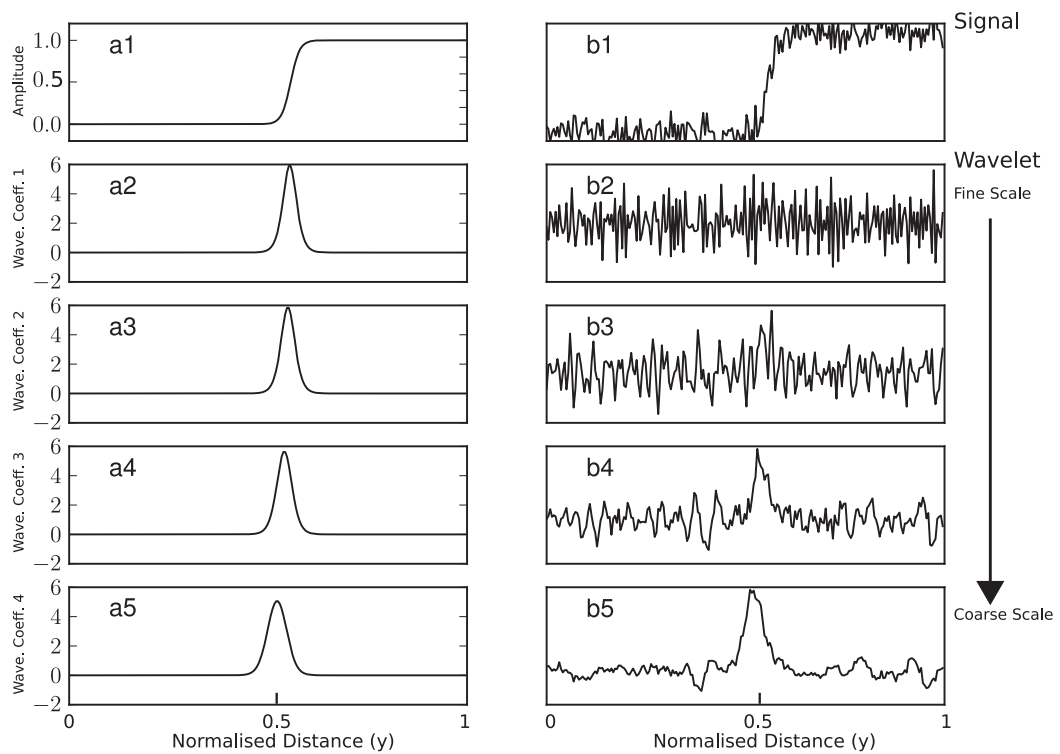


**Figure 2.** (a1) An example step signal with a finite rise time; (a2–a5) the discrete (undecimated) wavelet coefficients for the first four scales (using a Haar basis); (b1) same step signal with the addition of random Gaussian white noise with a signal-to-noise ratio of 20 dB; (b2–b5) the wavelet coefficients for the first four scales. The solid arrow indicates the direction of increasing scale, from fine scales to coarse scales.

to remove the noise by filtering, although this can blur the underlying signal. At best, the blurring induced by filtering can reduce the accuracy of the position of the detected step. At worst, as noise and steps frequently occupy similar locations in frequency space, filtering can remove the signal along with the noise, resulting in undetected steps.

These issues led to the development of many different methods. Here we discuss two: wavelet analysis and higher order statistics.

### 2.1.1. Wavelet Methods for Step Detection

The development of wavelet analysis led to new methods for the detection of steps. In a manner similar to Fourier analysis, wavelets allow a signal to be broken into its composite frequencies or “scales” [Farge, 1992]. However, Fourier analysis is a global decomposition; while it can tell us which scales (or frequencies) are present in the signal all information about when (or where) those frequencies occur is lost. Wavelets allow a time/frequency (or space/scale) decomposition: we can see which scales occur in a signal and where they occur in space or time [Farge, 1992; Percival, 2008].

Noise and some localized features are generally scale dependent: that is, noise is uncorrelated across scales. By contrast, steps and edges appear in several different scales, as shown in Figure 2. The same example step signals with and without noise from Figure 1 are used (shown in Figures 2a1 and 2b1), and the first four scales of wavelet coefficients (more precisely, the wavelet (detail) coefficients for an undecimated Haar wavelet) are shown in Figures 2a2–2a5 for the uncorrupted case, and in Figures 2b2–2b5 for noisy case. The wavelet coefficients at that first decomposition level (Figures 2a2 and 2b2) are a representation of the finest scale that can exist in the signal, variations with scales of  $2\Delta x$ . The wavelet coefficients corresponding to the coarsest scale are shown in Figures 2a5 and 2b5.

We can see that, in the noiseless case, all wavelet coefficients show maxima around the location of the step. However, in the noisy case, the wavelet coefficients corresponding to the finest scale (Figure 2b2) are dominated by noise. For the next smallest scale, shown in Figure 2b3 begin to show evidence of the step location. At the coarsest scales, the location of the step is clear to the eye (Figures 2b4 and 2b5). The signal

shows substantial correlation across scales, while the noise does not. The fact that the signal is present in multiple scales suggests a method for the separation of steps from noise: tracking wavelet maxima across scales.

*Mallat and Zhong* [1992] used wavelets to determine the location of edges in digital images by estimating Lipschitz exponents (a measure of correlation across scales) while *Sadler and Swami* [1999] made use of pointwise multiscale products, which acts to enhance the parts of the signal, which are correlated across different scales, and to suppress the uncorrelated (noisy) components. Wavelet results improve upon the filtered first derivative results both in terms of accuracy of the step location and in the reduction of false positives [*Carter et al.*, 2008].

### 2.1.2. Higher Order Statistics

Higher order statistics (HOS) generally refers to the analysis of signals using moments of order greater than two. Common examples include the third statistical moment (skewness), which is a measure of the “symmetry” of a distribution, and the fourth statistical moment (kurtosis), which is a measure of the “peakiness” of the distribution [*Lacoume et al.*, 1997]. These statistics are of interest as they can characterize the Gaussianity, or otherwise, of a signal.

Consider a length  $N$  signal  $x_t$ , where  $t \in [0, N-1]$ . The normalized Fisher kurtosis (sometimes called the “excess kurtosis,” and herein referred to simply as the “kurtosis”) of  $x_t$  is estimated by:

$$K(x) = \frac{\frac{1}{N} \sum_{i=1}^{N-1} (x_i - \bar{x})^4}{\left( \frac{1}{N} \sum_{i=1}^{N-1} (x_i - \bar{x})^2 \right)^2} - 3 \quad (1)$$

A Gaussian process has a kurtosis of  $\sim 0$ . To determine the Gaussianity of  $x_t$ , it is necessary to compare its  $K(x)$  with zero. Given the finite sample size of  $x_t$  and the fact that there are errors in the estimation of the kurtosis in equation (1), in practice we must specify a confidence interval. Should the value of  $K(x)$  be close enough to zero, the signal is taken to be Gaussian. A simple test of this kind was developed by *Ravier and Amblard* [1998] using the Bienaymé-Chebyshev inequality, which bounds the probability,  $Pr$ , that values of the sample kurtosis  $K$ , as estimated by equation (1) lie more than  $a$  standard deviations from the exact kurtosis (where  $a$  is a real number):

$$Pr(|K(x)| \geq a \sqrt{\text{Var}\{K(x)\}}) \leq 1 - \frac{1}{a} \quad (2)$$

*Ravier and Amblard* [1998] write  $a = \sqrt{1-\alpha}$ , where  $\alpha$  is the user selected *confidence parameter*, which is expressed as a fraction. The variance of the kurtosis estimator (equation (1)), if  $x_t$  is a Gaussian noise process, is

$$\text{Var}\{K(x)\} \approx \frac{24}{N} \quad (3)$$

for sufficiently large  $N$ . Combining equations (2) and (3), allows us to determine the interval in which the estimated kurtosis must lie if the signal is to be considered Gaussian:

$$|K(x)| < \frac{1}{\sqrt{1-\alpha}} \sqrt{\frac{24}{N}} \quad (4)$$

For example, with  $\alpha = 90\%$ , there a 90% probability that the estimated kurtosis of Gaussian process is no more than  $\sqrt{24/N(1-\alpha)} \sim 3\sqrt{24/N}$  greater or less than 0. Hence, if  $K(x)$  lies within the bounds given by equation (4), it is statistically indistinguishable from Gaussian noise. Should  $K(x)$  lie outside the bounds of equation (4), then  $x_t$  is unlikely to be Gaussian, with a confidence of  $\alpha$ .

HOS are useful for separating the “signal” and “noise” components of data. For example, if the “signal” is non-Gaussian (such as a step or pulse) while the noise is Gaussian (for example, a pseudorandom colored

noise process), HOS can be used to separate these two signal components. These methods are reviewed in detail in *Mendel* [1991] and *Lacoume et al.* [1997]. Both references show robust suppression of noise and retention of step-like signals.

The application of HOS to step detection is discussed in the articles of *Ravier and Amblard* [2001] and *Alyt et al.* [2006]. Both papers use wavelet-packet transforms alongside HOS. At each wavelet scale, the kurtosis is estimated and the wavelet coefficients at that scale are determined to be either Gaussian or non-Gaussian using equation (4). Noise is assumed to be Gaussian while steps are non-Gaussian. If Gaussianity is detected, that scale is assumed to be primarily noise and all wavelet coefficients are set to zero. Non-Gaussian coefficients are kept without change. Thresholding Gaussian scales acts to separate the noise from the step-like signal. After noise suppression, standard gradient thresholding methods can be employed to detect the location of the step. The results presented in *Ravier and Amblard* [2001] suggest that this method is able to preserve step-like features after denoising, even when SNRs are low.

## 2.2. Detection of Oceanographic Jets Using Wavelets and Kurtosis Thresholding

We now seek to apply the step detection methods described above to the problem of detecting oceanographic jets. Our methodology broadly follows *Ravier and Amblard's* [2001] technique for detecting steps in acoustic signals and shares some similarities with techniques for the detection of ocean eddies that exploit the scale-independence of sharp gradients in a wavelet transform [*Siegel and Weiss*, 1997; *Luo and Jameson*, 2002; *Doglioli et al.*, 2007]. There are also similarities with *Hughes et al.* [2010], who employed HOS to identify jets in the ocean. However, their method makes use of statistics computed in time, whilst our method makes use of statistics computed in space.

We note that our method differs from *Ravier and Amblard* [2001] and *Doglioli et al.* [2007] in several ways, primarily in the use of the undecimated discrete wavelet transform [*Fowler*, 2005], in place of the wavelet packet transform, as the latter decimates or "downsamples" the signal: removing samples in a manner consistent with the Shannon sampling theorem to ensure that no information in the signal is lost [*Smith*, 2003, p. 39]. As decimation reduces the number of samples in the wavelet coefficients at each scale, which in turn reduces the accuracy at which one can estimate properties such as kurtosis. Additionally, the noise thresholding component of *Doglioli et al.* [2007] is implemented iteratively, while our noise suppression steps are not.

In order to search for a jet, we must first have an idea of what we are looking for. As noted in section 1, there is no universally accepted definition of a jet in fluids. For the purposes of this paper, on a two-dimensional Cartesian grid with zonal and meridional coordinates  $x$  and  $y$ , we assume that a jet:

1. Manifests as a "step" in a particular geophysical field  $\eta(x, y; t)$ . In the ocean, this field is likely SSH, SST, potential vorticity or isopycnal interface height;
2. Near the jet  $\eta$  is assumed to vary more quickly in meridional direction than the zonal direction. That is,  $|\frac{\partial\eta}{\partial y}| > |\frac{\partial\eta}{\partial x}|$ . Note that this assumption does not preclude meanders or nonzonality in jets, only that the meander scales will be larger than the across jet scale.

The first assumption is used as a definition: a jet is a region with a locally high  $\eta$  gradient. The second assumption is used to separate jets from eddies, which can also manifest as sharp meridional gradients in  $\eta$ , but generally have a restricted zonal scale. For jets in the midlatitude ocean and atmosphere, the meridional width  $Y_{jet}$ , generally scales with the first baroclinic deformation radius:  $Y_{jet} \sim R_d$  [*Dritschel and McIntyre*, 2008]. However, jets persist in the zonal direction for scales much larger than  $R_d$ . In contrast, eddy scales in both zonal and meridional directions scale with the deformation radius:  $Y_{eddy}, X_{eddy} \sim R_d$ . This scale separation gives us a criterion by which we can differentiate between eddies and jets.

We now describe our algorithm, which we explain with the aid of the "toy" problem introduced in section 2.1. The stages of the algorithm are illustrated in Figure 3. Figure 3a shows the initial signal: an idealized step with the addition of pseudorandom Gaussian white noise. The SNR is 20 dB. The idealized step in Figure 3a is analogous to a meridional transect of SSH. The stages of our algorithm are:

1. Smooth in the zonal (along jet) direction at a cutoff wave number  $k_{cutoff}$  in order to separate eddies and jets. Smoothing would be performed in the *out of the page* direction in Figure 3;

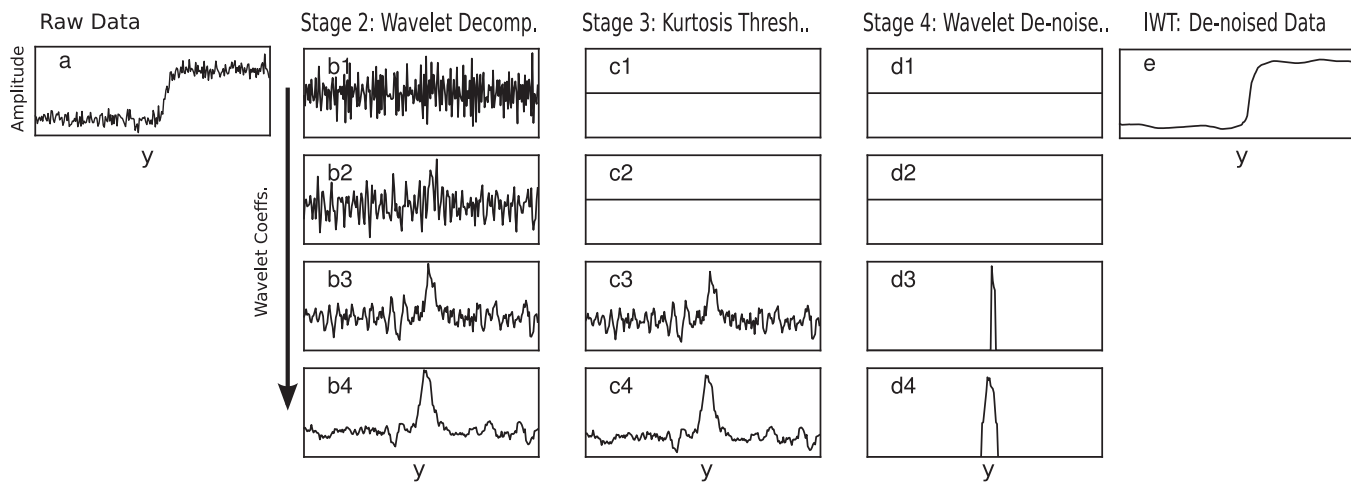


**Figure 3.** The noise suppression and step detection procedure: (a) the original noisy signal; (b1–b4) stage 1: the discrete (undecimated) wavelet coefficients for the first four scales; (c1–c4) stages 2 and 3: kurtosis thresholding. The wavelet coefficients in Figures 3c1 and 3c2 have a kurtosis less than the threshold, and are set to zero. Those in Figures 3c3 and 3c4 have kurtosis above the threshold and are retained; (d1–d4) stage 4: wavelet denoising. Wavelet coefficients with small magnitudes are set to zero; and (e) the reconstructed signal obtained from the Inverse Wavelet Transform (IWT) after denoising. The arrow indicates the direction of increasing scales within the wavelet decomposition, from fine scales to coarse scales.

2. Perform the discrete wavelet decomposition on each meridional transect, at each time step (here, we use the Haar wavelet). The wavelet coefficients for the idealized step are shown in Figures 3b. It can be seen that the wavelet coefficients in Figures 3b1 and 3b2 (which correspond to finer scales) have a more noise-like character, while those in Figures 3b3 and 3b4 (coarser scales) show a pronounced peak in the center of the domain that corresponds to the location of the step in Figure 3a;
3. At each scale, determine the kurtosis of the wavelet coefficients and apply equation (4) to determine the Gaussianity at that scale. Scales determined to be Gaussian are set to zero. Non-Gaussian scales are kept without modification. Figures 3c show the result of the kurtosis thresholding. The “noisy” coefficients (Figures 3c1 and 3c2) vanish while the coefficients that show the pronounced peak at the step location (Figures 3c3 and 3c4) are unchanged;
4. Apply a standard wavelet denoising process to further increase the SNR.

Wavelet denoising is a simple process [Taswell, 2000], but requires some explanation here: for the wavelet coefficient,  $d^s(x_i, y; t)$ , for scale  $s$ , along a transect located at longitude  $x_i$ , if the absolute value of the coefficient at point  $y=y_j$  is less than a predefined threshold parameter  $\lambda^s$ , it is set to zero. Otherwise, it is retained unchanged. This is essentially the process used by Siegel and Weiss [1997] and Doglioli *et al.* [2007] in their eddy detection algorithms. In this study, we choose  $\lambda^s$  to be the threshold of Donoho and Johnstone [1994]. For the  $i$ th meridional transect,  $\lambda^s$  is set to:

$$\lambda_i^s = \frac{\text{median}\{|d^s(x_i, y; t)|\}}{0.6745} \sqrt{2 \log_{10} N_y} \quad (5)$$

where  $N_y$  is the number of points along the transect. Wavelet denoising is shown in Figure 3d. Wavelet coefficients with small magnitudes are set to zero. Wavelet coefficients with large magnitudes are retained. We see in Figures 3d3 and 3d4 that the coefficients that are retained in our simple example are those corresponding to the large peak in the center of the domain;

5. Reconstruct the signal using the modified wavelet coefficients and the inverse wavelet transform. For our simple example, this is shown in Figure 3e;
6. Finally, use a “standard” method, such as gradient thresholding or multiscale products to locate steps.

In the problem illustrated in Figure 3, Figure 3a represents the initial, noisy signal, while Figure 3e is the final product: a step signal separated from the noise. We can see by comparing Figures 3a and 3e that once the methodology described above has been applied, the noise has been almost entirely suppressed, while the signal has retained its step characteristic.

The principles of the method are the same as gradient thresholding: identify regions of high  $\eta$  gradients. The value of our new method is that it improves the SNR; reducing the impact of eddies while retaining jets. Our new method should be seen as an enhancement to the existing gradient thresholding methods; hence, we name the method the Wavelet/HOS Enhancement (WHOSE).

### 3. Comparison of Jet Detection Methods Using Synthetic SSH Fields

In this section, we quantitatively compare the WHOSE method proposed in section 2.2 with three commonly used jet detection methods:

1. Gradient thresholding methods described in *Graham et al.* [2012];
2. PDF methods described in *Thompson et al.* [2010];
3. Contour methods, with the implementation taken from *Volkov and Zlotnicki* [2012].

#### 3.1. Synthetic Data Generation

In order to compare these techniques in a quantitative manner, we generate a pseudorandom SSH field that shares some features of the observed SSH in the Southern Ocean. The advantage of this approach, as opposed to using data directly from observations or numerical output, is that we know the exact position of jets a priori, allowing us to compute error statistics.

To begin, we generate a two-dimensional jet, with a simple meridional SSH profile given by:

$$\eta(y)_{\text{jet}} = \Theta \tanh\left(\frac{y - y^*(x)}{Y}\right) \quad (6)$$

where  $\eta$  is the SSH,  $\Theta$  is the (constant) step amplitude,  $y^* = y^*(x)$  is the meridional location of the jet core at  $x$ , and  $Y$  is the step width.  $y^*(x)$  varies with longitude in a simple manner:

$$y^*(x) = \mathcal{Y} \sin(\ell x) \quad (7)$$

where  $\ell$  is the zonal wave number of the jet meander and  $\mathcal{Y}$  is the (constant) meander amplitude.

These synthetic jets constitute the “mean” field  $\bar{\eta} = \eta_{\text{jet}}$ . To this mean field, we add a synthetically generated eddy field  $\eta'$ . The synthetic eddies are a two-dimensional pseudorandom field generated following *Wu* [2000]: a 2-D spectrum is provided as an input. Using the analysis of eddy scales by *Xu and Fu* [2011], we choose a isotropic power law spectrum with a slope of 11/3. We then randomize the phase angles of the 2-D spectrum and apply an inverse Fourier transform to return a 2-D pseudorandom field. The amplitude of the resulting eddy field is scaled to give a chosen signal-to-noise ratio (SNR), defined as:

$$\text{SNR} = 10 \log_{10} \left( \frac{\Theta}{\text{RMS}\{\eta'\}} \right) \quad (8)$$

where  $\text{RMS}\{\eta'\}$  is the root-mean-squared value of the eddy field. The SNR is reported in decibels (dB).

We use a grid with  $N_x = 512$  grid points in the  $x$  direction, and  $N_y = 256$  grid points in the  $y$  direction, a grid spacing of  $\Delta x, \Delta y = 10$  km. The single jet has an amplitude  $\Theta = 10$  cm, width  $Y = 3\Delta y$ , selected in order to give maximum current speeds  $\sim 1$  m s $^{-1}$  and jet widths of  $\sim 50$ –100 km, which are representative of observed values in the Southern Ocean [*Gille*, 1994; *Sokolov and Rintoul*, 2007]. We have chosen meanders of wave number 2, with an amplitude of  $10\Delta y = 100$  km. Finally, we add a uniform slope in the  $y$  direction to the SSH field, with a difference of 50 cm between the northern and southern boundaries to better approximate the observed SSH in the Southern Ocean. An example SSH field and its associated speed field is shown in Figure 4.

The SSH field in Figure 4 resembles some features of the SSH field observed from altimetry [*Morrow and Le Traon*, 2012]. We note that distribution of SSH of the synthetic eddy field has a Gaussian PDF, which is not the case everywhere in the ocean. In addition, our eddies are distributed homogeneously throughout the

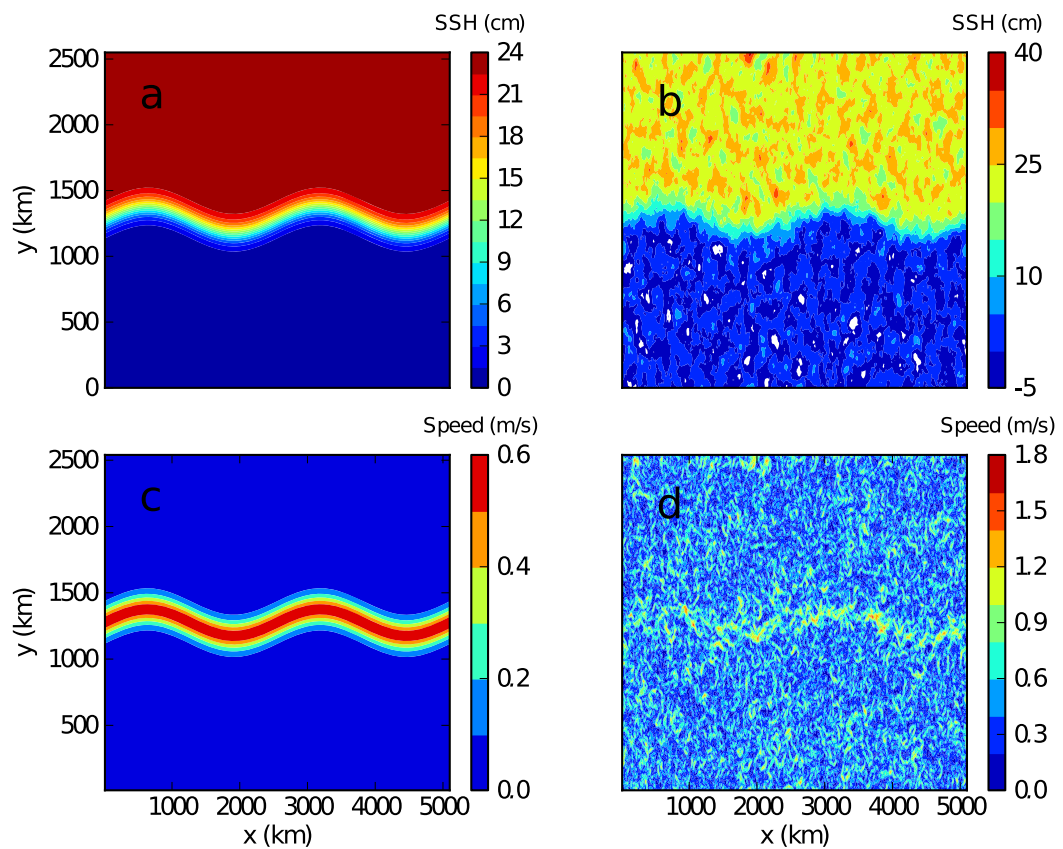


**Figure 4.** An example of a synthetic sea-surface height field (a) mean synthetic SSH field; (b) mean synthetic SSH with the addition of eddies ( $\text{SNR} = 10 \text{ dB}$ ); (c) mean synthetic speed field derived from Figure 4a; and (d) mean speed with the addition of eddies, derived from Figure 4b.

domain, which is not the case in the ocean. Areas of anomalously high eddy activity are found in the wake of large topographic features and along the cores of jets [Williams *et al.*, 2007].

### 3.2. Implementation Details

In implementing the gradient thresholding, WHOSE and PDF methods, we have employed a spatial low-pass filter to smooth the SSH fields. We use a windowed sinc filter with a Blackman Window, described in [Smith, 2003, p. 285], with a cutoff wavelength of  $5\Delta x$  (50 km) in the  $x$  direction for the WHOSE and PDF methods. When applying standard gradient thresholding, we have found through experimentation that cut-off wavelength must be larger ( $\sim 10\Delta x = 100 \text{ km}$ ), and that smoothing must be applied in both the  $x$  and  $y$  direction. The cutoff wavelength was determined by repeated testing of the each method on high SNR data sets while simultaneously attempting to eliminate or reduce the number of false positive jet identification events and use the smallest cutoff wavelength possible. Smoothing is not performed for the contour method.

Gradient thresholding was implemented by first smoothing the SSH field in both  $x$  and  $y$  directions, then computing the gradients. Derivatives were calculated using a five-point central difference stencil to reduce speed-dependent bias [Arbic *et al.*, 2012]. Gradient maxima were then identified using an adaptive peak detection algorithm that compares the magnitude of local maxima to the magnitude of the values in the surrounding neighborhood (a  $10\Delta x \times 10\Delta x$  box). If the difference in magnitude between the peak and the surrounding neighborhood exceeds a predefined threshold, then that local maximum is accepted as a jet location; otherwise it is assumed to be small-scale noise and rejected. The value of this threshold must be found by trial and error.

For the PDF method, after smoothing, a sliding window histogram is computed. The width of this window was set to  $0.1 N_x$ , selected to provide a balance between zonal resolution and the collecting a sufficient

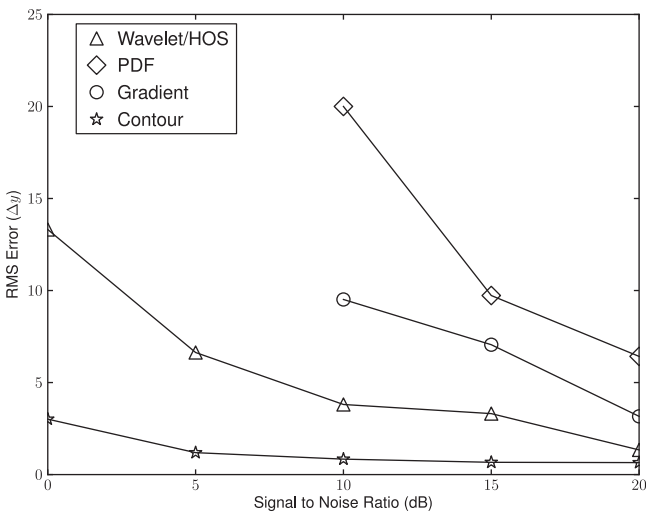


**Figure 5.** The mean RMS error of the four jet detection methods at varying signal-to-noise ratios. “Triangle” denotes the WHOSE method, the “circle” the gradient threshold method, “diamond” the PDF method, and the “star” the contour method.

Bienaymé-Chebyshev inequality (equation (4)) to 0.9.

The contour method was implemented following Volkov and Zlotnicki [2012]: we integrate the square of the SSH gradient (computed by finite differences) along contours of SSH. Local maxima in this field were identified as jets computed using the same adaptive peak detection method described above.

### 3.3. Comparison of Jet Detection Methods

To compare the four jet detection methodologies, we use a Monte-Carlo approach. For a given SNR, we generate 500 synthetic SSH fields, consisting of the mean jet and 500 unique pseudorandom eddy fields, which we have found to be a sufficient number of tests to generate useful error statistics. For each synthetic SSH field, we compute the root mean squared error:

$$RMSE = \left[ \frac{1}{N_x} \sum_i^{N_x} (y^*(x_i)_{\text{detected}} - y^*(x_i)_{\text{true}})^2 \right]^{1/2} \quad (9)$$

All RMS error results have been bias corrected, so that they are representative of random scatter. Bias was small in all methods, being restricted to less than  $3\Delta y$  for all cases and found to be independent of SNR.

We then apply the four jet detection methods to each of these SSH fields and compute the RMS error. This procedure can then be repeated for different SNRs, allowing us to quantify the performance of each method as the SSH fields become more dominated by eddies. The mean RMS errors of the 500 individual synthetic SSH fields are shown in Figure 5. Each method shows a decrease in mean RMS error as the SNR increases. At high SNRs (10–20 dB), we find that all four methods are able to robustly determine the jet location: that is, for each of the 500 synthetic SSH fields, there are sufficiently few false positives, and the detected points are clustered sufficiently close together that a single jet feature can be identified. However, we find that as the SNR decreases, both the PDF and gradient thresholding method struggle to distinguish the jets from the eddy field. Experimentation has found that both these methods fail as the SNR decreases below  $\sim 10$  dB.

In comparison to the gradient thresholding and PDF methods, both the WHOSE and contour methods perform well at a low SNRs with jets still being detected even with an SNR of 0 dB. The WHOSE method has improved accuracy at low SNRs when compared to both the gradient thresholding and the PDF methods. The contour method shows superior accuracies at all SNRs, with RMS errors remaining below  $5\Delta y$ , which is approximately the jet width. The accuracy of the WHOSE method degrades faster than that of the contour

number of points to form meaningful PDFs. The minima in the PDF were detected using the same adaptive peak detection algorithm as was employed in gradient thresholding, reconfigured to search for minima. These minima were then mapped back into geographic coordinates to denote the jet locations.

The WHOSE method was implemented, following the steps presented in section 2. After the SSH field has been processed using the WHOSE methodology, gradient thresholding is applied to the denoised SSH as described above. We set the confidence parameter,  $\alpha$ , in the

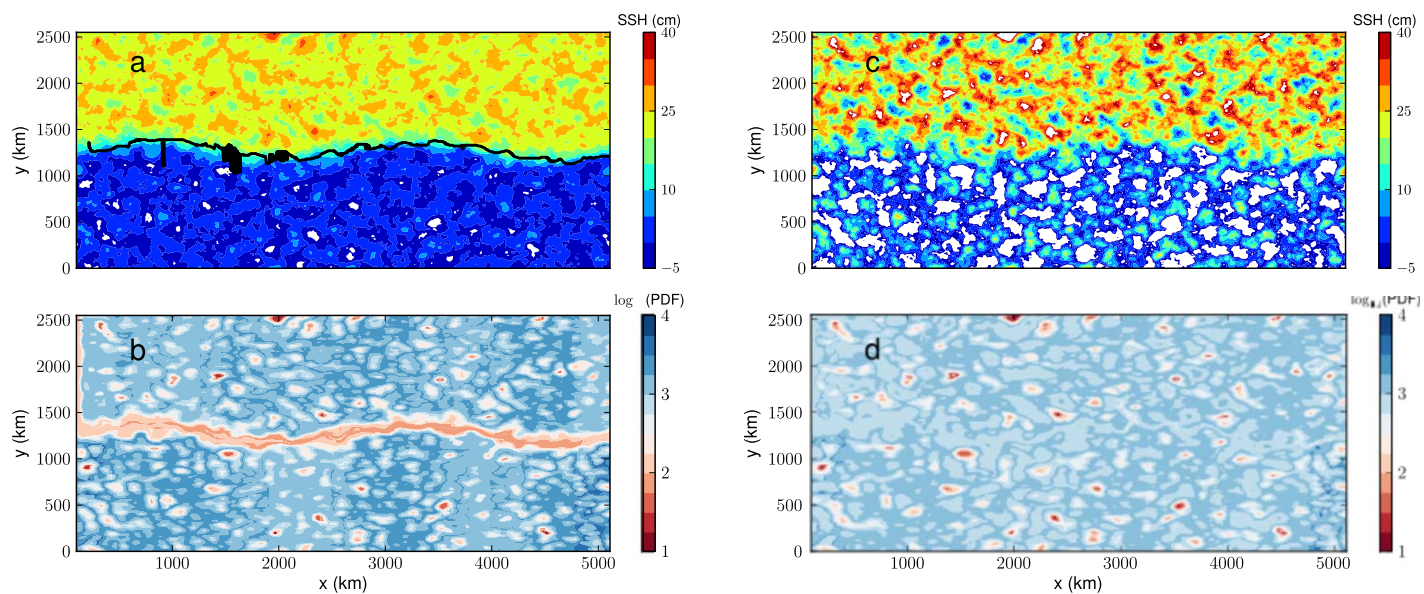


**Figure 6.** Examples of the PDF method of Thompson et al. [2010] applied to a synthetic SSH field with different SNRs. (a) SSH field (SNR of 20 dB); (b) resulting spatially mapped histogram (SNR of 20 dB); (c) as in Figure 6a, but with an SNR of 10 dB; (d) as in Figure 6b, but with SNR of 10 dB. Black lines in Figure 6a show detected jet locations.

method as the SNR decreases. In Figure 5, we see that at an SNR of 0 dB, the average RMS error of the contour method is less than half that of the WHOSE method.

Gradient thresholding shows reasonable results at SNRs greater than 15 dB with errors less than  $10\Delta y$ . However, we note that the SSH field must be smoothed in both zonal and meridional direction in order to distinguish jets from eddies, particularly at lower SNRs. Without smoothing, gradient thresholding reports many false positives as local eddy-induced SSH gradients can be of similar magnitude those associated with the jet. Both the PDF method and the WHOSE method only require smoothing in the zonal direction.

Like simple gradient thresholding, the PDF method fails to detect jets at SNRs lower than 10 dB. The reasons for the failure of gradient thresholding were discussed in detail in section 2. The PDF method fails at lower SNRs due to the fact that eddies have a similar representation in a histogram as do jets, demonstrated in Figure 6. Figure 6a shows a single SSH instance with a high SNR (in this case 20 dB) and Figure 6b shows its representation as a spatially mapped histogram. The location of the jet is clearly seen in Figure 6b as a region of low PDF values lying between two homogenized SSH regions. Figures 6c and 6d are identical to Figures 6a and 6b, except that an SNR of 10 dB has been used. In Figure 6d, there is an apparent PDF minima roughly following the jet core, although it is no longer as distinct from the surrounding homogenized regions when compared with the higher SNR case. This results in the PDF minima being more difficult to distinguish from its surroundings. As the SNR decreases, this effect leads to the failure of the method.

Of all four methods tested, the contour method has the lowest error at all SNRs. However, the superior error performance of the contour method should not be taken to mean it is recommended in all cases. The synthetic jet used in this section is particularly suited to detection via the contour method, as the jet core remains, by equation (6), on a single SSH contour. The criticisms of contour methods in Thompson et al. [2010] and Graham et al. [2012] are concerned with the impact of a jet straying off the SSH contour. We have not tested for this effect in this study. Should it occur, it would undoubtedly reduce the accuracy of the contour method. From these results, we can say that the accuracy of contour methods is relatively insensitive to the eddy field provided that the jet cores remain confined to the SSH contour.

To summarize the results of this section, we have shown that at high SNRs (15–20 dB), all four methods tested in this study have similar accuracies. At lower SNRs (10–15 dB), three methods (gradient thresholding,

PDF and the WHOSE) become less accurate while the accuracy of the contour method only reduces a small amount. The PDF and gradient thresholding methods show a much greater reduction in accuracy when compared to the WHOSE and contour methods. At SNRs less than 10 dB, the WHOSE and contour methods continue to detect jets, albeit at a reduced accuracy, while the other two methods tested here fail to detect jets at all. We conclude that in regional or very high resolution studies either the WHOSE method or the contour methods may be preferable to gradient thresholding or PDF methods.

#### 4. Comparison of Jet Detection Methods in a High-Resolution Model

In the previous section, we showed that the accuracy of each jet detection method degrades as the magnitude of the noisy “eddy” flow increases relative to the magnitude of the mean flow. This result has implications for the application of these methods to data from remotely sensed observations or numerical models. In general, as the horizontal resolution of a data set increases, the data fields become more “eddy rich.” Resolution will also influence the structure of jets, with higher-resolution data sets forming stronger, narrower and more variable jets [Hallberg and Gnanadesikan, 2006]. As computing power increases and observational data sets become more refined, higher-resolution data sets are fast becoming the norm rather than the exception. Additionally, certain regions of the ocean are more eddy rich than others [Thompson and Richards, 2011], meaning that some methods may fail to accurately identify jets in those regions, even if they provide accurate results in regions with a weaker eddy field. How do different jet detection methodologies perform in high-resolution data sets? In this section, we apply several jet detection methodologies to the output of an eddy-resolving numerical model to answer this question.

##### 4.1. Description of the Ocean Model Output and Determination of the SNR of the Southern Ocean

We use output from the Ocean General Circulation Model for the Earth Simulator (OFES) [Masumoto *et al.*, 2004], which has a horizontal grid spacing of  $1/10^\circ$ . At representative Southern Ocean latitudes (from  $35^\circ\text{S}$  to  $60^\circ\text{S}$ ), this grid spacing is of similar order to the first baroclinic deformation radius ( $\sim 10\text{--}20$  km), which is generally considered eddy resolving. The output of this model has been examined by Thompson and Richards [2011] and Thompson *et al.* [2010], who found that it produces an eddy-rich Southern Ocean which forms a number of realistic, variable jets. They concluded that this model is consistent with other high-resolution simulations and observations of the Southern Ocean.

We analyze data for the year 2005. These data are provided as 3 day snapshots giving a total of 122 records. The year 2005 is chosen arbitrarily, although repeating the analysis using different years or for longer time periods does not appreciably change the results. We have chosen to restrict our attention to Southern Ocean latitudes between  $35^\circ\text{S}$  and  $65^\circ\text{S}$  and the eastern hemisphere of longitudes between  $0^\circ$  and  $180^\circ$ . The ocean bottom topography from the ETOPO1 data set [Amante and Eakins, 2009] for the region is shown in Figure 7a, with key features labeled.

In order to identify regions where the detection of jets may be difficult, we estimate the SNR of the model output in the Southern Ocean. To do this, we first define the “signal” as the time averaged free surface height gradient:  $|\nabla \bar{\eta}|$ , where the overline denotes the time average.  $|\nabla \bar{\eta}|$  for the year 2005 is shown in Figure 7b. The “noise” field is defined as the RMS of the anomaly gradient:

$\text{RMS}\{\eta'\}(x, y) = \sqrt{\frac{1}{N} \sum_t \left[ (\nabla \eta'(x, y; t))^2 \right]}$ , where  $\eta'(x, y; t) = \eta(x, y; t) - \bar{\eta}(x, y)$ . The RMS eddy gradient is shown in Figure 7c. Finally, we define the SNR as:

$$\text{SNR} = 10 \log_{10} \left( \frac{|\nabla \bar{\eta}|}{\text{RMS}\{\eta'\}} \right) \quad (10)$$

The computed SNR is shown in Figure 7d. In this figure, it can be seen over large portions of the domain, particularly in regions with strong  $|\nabla \bar{\eta}|$ , that the SNR typically falls between 10 and 20 dB. With reference to the results from the synthetic data (Figure 5), we infer that in regions with higher SNR, jets can be detected using either the gradient thresholding or PDF methods. The fact that in majority of regions with strong SSH gradients that the SNR lies between 10 and 20 dB partially validates the results of gradient thresholding in Hughes and Ash [2001] and Graham *et al.* [2012].

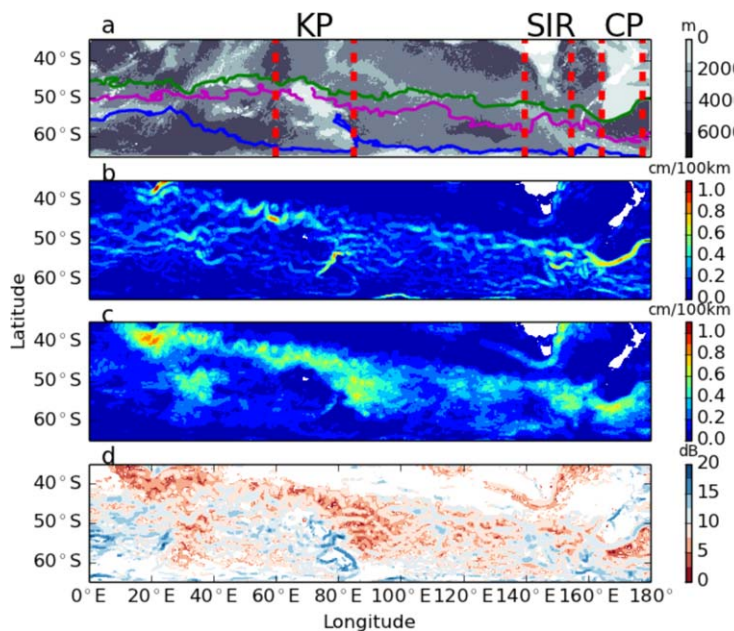


**Figure 7.** (a) Bottom topography from the ETOPO1 data set in the eastern hemisphere of the Southern Ocean. Solid lines indicate the location of the Sub Antarctic Front-Mid (green), the Polar Front (magenta), and the Southern ACC front (blue) computed from subsurface temperature criteria; (b) time mean free surface height gradient; (c) RMS eddy gradient; and (d) the SNR calculated by equation (10). Note that in Figure 7d, regions where the gradient magnitude is less than 0.05 cm/100 km have been masked. All quantities computed from the OFES model output for the year 2005. Longitudes of the Kerguelen Plateau (KP), Southeast Indian Ridge (SIR), Campbell Plateau (CP) are indicated by the red dashed lines. Note the inverse color scale in Figure 7d.

Figure 7c shows that the eddy field in the OFES output is spatially inhomogenous. In regions with a strong eddy field and weak time mean gradients, the SNR falls  $\sim 0$  dB. Particular regions with low SNRs are downstream of the Kerguelan Plateau (centered at approximately  $70^{\circ}$ E,  $50^{\circ}$ S, label “KP” in Figure 7a), and near the Southeast Indian Ridge (from  $140^{\circ}$ E to  $160^{\circ}$ E, label “SIR” in Figure 7a). It is interesting to note that in the Campbell Plateau region (from  $170^{\circ}$ E to  $180^{\circ}$ E, labels “CP” in Figure 7a) although the eddy field is strong, the SNR is still high, due to the strong mean jet in that region. In the low SNR regions, standard gradient thresholding and the PDF method should not be expected to work well, given the results of section 3. However, we might expect that contour methods and the WHOSE method might continue to identify jets in the low SNR regions.

Finally, to provide a simple comparison of the methods discussed here with those from hydrography, we have used the temperature criteria of *Langlais et al.* [2011] to define three hydrographic fronts (the mid branch of the Subantarctic Front, the Polar Front, and the Southern ACC front) that correspond to those described by *Orsi et al.* [1995]. The time mean locations of these fronts are shown in Figure 7a. These frontal locations provide a link to the “traditional” view of Southern Ocean fronts. It should be noted that the contour methods of *Sokolov and Rintoul* [2007] were found to be consistent with the results of *Orsi et al.* [1995].

#### 4.2. Comparison of Jet Detection Methods

We compare three jet detection methods: the WHOSE method, the PDF method, and the contour method. We have chosen not to test simple gradient thresholding in this section, since the WHOSE method is an enhancement to gradient thresholding and operates on the same principles. Each method is applied to the OFES free surface height field.

The three jet detection methodologies are each applied at every time step in the data set. From these computations, we build a time series of jet locations. As the WHOSE and the PDF methods do not define jets to be continuous in space, nor specify the number of jets *a priori*, unlike the contour method, care must be taken when following jets through time. Here we use a simple method to build a picture of the time evolution of jets in the OFES model: for each time step and grid point if a jet is present at that location, that grid point is flagged as “true.” If a jet is not present at that grid point, it is flagged as “false.” More formally, the time series can be written as a function  $P$  with binary output:

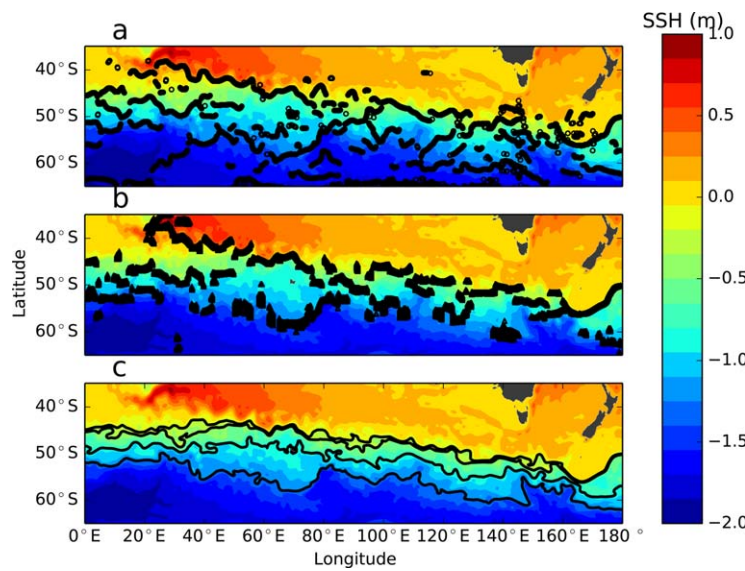


**Figure 8.** The 2005 annual average of the free surface height in the OFES model for the year 2005 with the estimated jet locations found using: (a) WHOSE (black "circle"); (b) PDF (black "triang:"); and (c) contour (black lines) methods.

$$c^K = P^K(x, y; t) \quad (11)$$

where  $c^K \in \{0, 1\}$  and  $K$  indicates the jet detection method used.

We can estimate both the variability and the time mean jet positions by summing  $P^K(x, y; t)$  along the time axis to form a “jet position histogram.” This operation counts the number of times a jet was present at a particular grid point throughout the data period. Meandering jets can be seen in histogram: mean positions of jets will be represented as local maxima in the histogram, while meandering jets can be seen as a distribution of lower values around those peaks. A sharp, localized peak indicates a jet with little time variability, while a more broad distribution of points around the peak indicates a meandering jet.

We define the time mean jet positions by tracking local maxima in jet position histogram. We have compared this approach to simply applying the jet detection methodologies to time mean SSH field, finding that the results, although not identical, are very similar.

When applying the contour method to the OFES data set, using the methodology of Volkov and Zlotnicki [2012], we are able to unambiguously identify four jets. It is possible to specify more jets although there is considerable uncertainty in choosing SSH contours.

#### 4.2.1. Time Mean Jet Positions

Figure 8 shows annual mean of the SSH gradient of the OFES model output for the year 2005, computed in a Mercator coordinate system which implicitly accounts for the variations in distance along longitude lines due to the sphericity of the Earth. The mean annual jet positions for the WHOSE method, the PDF method and the contour method are shown in Figures 8a, 8b, and 8c, respectively. The methods are implemented as described in section 3. All methods use the free surface height field as an input.

In the time mean, the three methods show broad agreement in placing the jets, consistent with the positions of the hydrographic fronts obtained using temperature criteria, shown in Figure 7a. Agreement between methods is particularly strong in regions where jets are strongly steered by topography. There are two primary examples of this: the Kerguelen and Campbell plateaus.

The Kerguelen Plateau (label “KP” in Figure 7a) is a large topographic feature known to steer Southern Ocean jets [Park *et al.*, 2008]. The jet associated with the Subantarctic Front is known to pass to the north of the Kerguelen Plateau [Park *et al.*, 2008; Sokolov and Rintoul, 2009a]. There is some controversy about the location of the jet associated with the Polar Front with various sources placing it to the south of Kerguelen Island where it passes through the Kerguelen Island Trough at 71°E, 51°S or to the north of the plateau, merging with the strong jet there [Roquet, 2009].

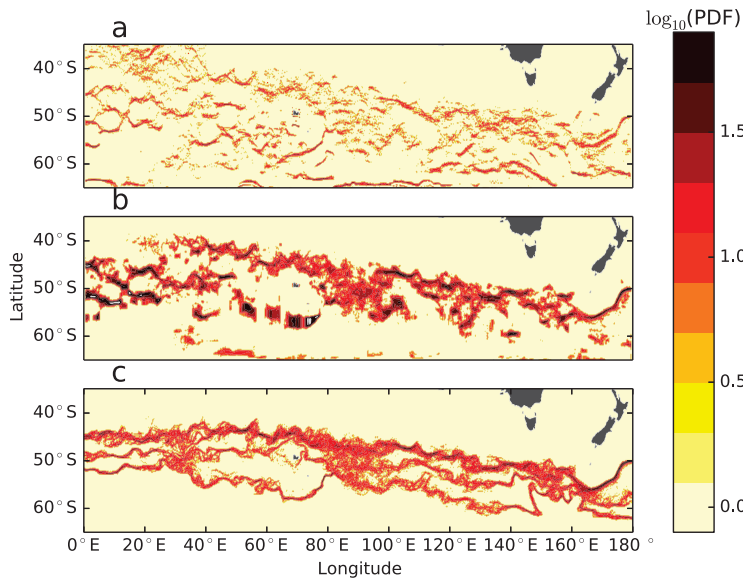


**Figure 9.** Jet position histograms described in section 4.2 in the eastern hemisphere of the Southern Ocean, computed using the: (a) WHOSE; (b) PDF; and (c) contour methods. Warm colors indicate more persistent jets. Note the logarithmic color scale.

It can be seen in Figure 8 that the three methods show a strong, persistent jets both to the north of the Kerguelen Plateau and to the south, where a jet passes through the Fawn Trough, which is consistent with the currents described in Park *et al.* [2008]. There is some divergence between methods regarding the flow through the Kergulean Island Trough. Both the WHOSE and contour methods place a jet at this location which is not detected by the PDF method.

The Campbell Plateau, which lies to the south of New Zealand at approximately 170°E, 55°S (label “CP” in Figure 7a) is also known to strongly steer jets [Langlais *et al.*, 2011]. We can observe this steering in the SSH gradient field in Figure 7b, which shows a continuous strong gradient with significant curvature spanning longitudes from about 160°E to 180°. All three methods place a jet in this location. There is strong agreement between the methods to the south of the Campbell Plateau as well, with the three methods each placing additional jets following strong SSH gradients at approximately 60°S, although the longitudinal extent of the jets in this region varies between methods. Despite these differences, the three methodologies present a similar overall picture in the placement of jets where they are strongly steered by topography. The three methodologies are also broadly consistent with the placement of fronts using temperature criteria, shown in Figure 7a.

In regions where the flow is not strongly steered by topography, there are notable differences between the methodologies in the placement of time mean jets. As a particular example, an abyssal plain between 10°E and 40°E has been identified by Sallée *et al.* [2008] and Langlais *et al.* [2011] as a region showing enhanced variability in frontal positions. In this region, both the WHOSE and PDF methods indicate a number of interleaved, braided jets. There is also evidence from these two methodologies of discontinuous jets that break at certain longitudes before reforming further to the east. The contour method reveals a different picture: a field of continuous, quasi-zonal jets that split and merge. Similar differences between the methodologies can be found downstream of the Kergulean Plateau between 80°E and 100° and in the region south of Australia between 120°E and 140°E, a region that follows the Southeast Indian Ridge a zonally oriented topographic feature known to strongly influence the behavior of Southern Ocean jets (label “SIR” in Figure 7).

#### 4.2.2. Time Variability

We now discuss the different results obtained by the three methodologies regarding the time variability of jets. Figure 9 shows the jet position histogram for the WHOSE method (Figure 9a), the PDF method (Figure 9b) and the contour method (Figure 9c). In Figure 9 “warmer” colors correspond to regions where a jet is found more frequently, while “cooler” colors are regions where the jet is found less frequently.

As in the case of the time mean jet position, there is substantial agreement between the three methods in certain regions, particularly where the flow is strongly steered by topography. For example, south of the

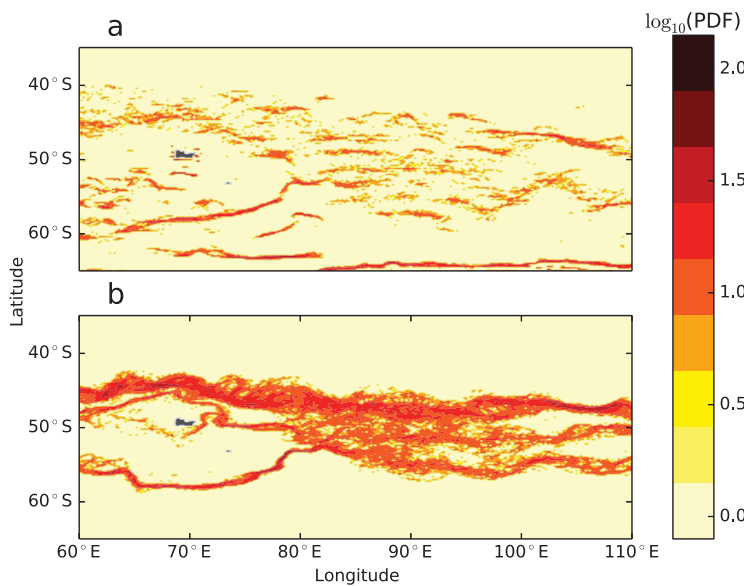


**Figure 10.** Jet position histograms described in section 4.2 downstream of the Kerguelan Plateau, computed using the: (a) WHOSE; (b) contour methods. Warm colors indicate more persistent jets. Note the logarithmic color scale.

Kerguelen and Campbell plateaus, and north of the Eastern Indian Ridge (located at 110°E, 48°S), the jet position histograms computed by all three methods show narrow distribution of points around these topographic features, indicating that jets in this region show little variability.

The three methods are also broadly in agreement in regions of enhanced variability. For example, downstream of the Kerguelen Plateau, between 80°E and 100°E, we observe a broad distribution of points in all three methods, indicating significant variability in jet locations, which is consistent with *Sallée et al.* [2008]. There is similar agreement in the jets variability downstream Southeast Indian Ridge.

There are several substantial differences between the methodologies. For example, south of Australia, between 110°E and 130°E, the PDF method has a much broader distribution of points, indicating substantially greater variability than the other two methods. In this region, SSH gradients are comparatively weak, giving a low SNR (Figures 7c and 7d). As described in section 3, the PDF method performs poorly in situation with a low SNR. In the region between 110°E and 130°E, the weaker gradients lead to the PDF method detecting a high number of false positives, resulting in an overestimate of the jet variability.

The WHOSE method differs from the other two methods in the region upstream of the Kerguelen Plateau at roughly 70°E, 55°S. The WHOSE method shows a number of braided, fine-scale jets. This region is characterized by numerous weak SSH gradients (Figure 7b), suggestive of weaker jets, yet is also a region of low eddy activity (Figure 7c). As can be seen in time mean (Figure 8a) the WHOSE method identifies numerous persistent jets in this region that are not identified by the other methods. The WHOSE method is likely detecting jets that are too weak to be identified by the other two methods.

Another significant difference between the three methods can be seen in the region between 0° and 30°E. All three methodologies show persistent jets with little to no variability. However, the trajectories followed by the jets in this region differ substantially between methods, with the WHOSE and PDF methods showing the braided, nonzonal structure alluded to in section 4.2.1, while the contour method gives more zonal jets with evidence of splitting and merging, a result more consistent with *Sokolov and Rintoul* [2009a].

As a more general comment, it can be seen in Figure 8, that the WHOSE method detects more fine-scale behavior than either the contour or PDF methods. To investigate this further, we look more closely at the region downstream of the Kerguelen Plateau, which has an active eddy field. In this region, Figure 7d shows that the SNR is  $\sim$ 0–10 dB, and hence, noting the analysis undertaken using the synthetic SSH fields, standard gradient thresholding and the PDF method, are not expected to work well. Figure 10 shows the jet position histograms for the WHOSE (Figure 10a) and the contour method (Figure 10b) in this region.

In Figure 10, we see that the WHOSE method shows a complex jet field, with a varying number of interleaving, discontinuous jets, consistent with the high resolution simulations of I. Rosso et al. (Vertical transport in the ocean due to sub-mesoscale structures: Impacts in the Kerguelen region, submitted to *Ocean Modelling*, 2014) and reminiscent of the quasi-geostrophic experiments of Thompson [2010]. The spatial histograms associated with these jets are oriented largely zonally, and do not show a broad distribution of points, suggestive of jets that are persistent geographically. Additionally, the magnitude of the jet position histogram indicates a relatively few occurrences of jets in these regions, indicating jets that are highly localized in space but with temporally variable strength. The highly fragmented, filamentary jet field suggests that the strong SSH gradients associated with a dynamical jet are discontinuous, both spatially and temporally.

In contrast, the contour method shows four continuous jets with evidence of meandering, splitting and merging, but without the complex braiding found by the WHOSE method. Closer to the topography (from 75°E to 95°E), the jets found by the contour method show more meandering than further downstream.

Comparing Figures 10a and 10b, it can be seen that strong SSH gradients are not found at all points along each of the SSH contours, a result consistent with the analysis of Graham et al. [2012]. As such, the meandering of the SSH contours in this region should not be taken to imply a meandering of the high SSH gradients, which the WHOSE method indicates are persistent at certain geographical locations, although with possibly temporally variable strength. The two different jet fields shown in Figures 10a and 10b may show different manifestations of the same variability: multiple jet filaments appearing with applications of the WHOSE method, and a meandering front with application of the contour method.

Similar differences between the detected jet fields can be seen in other low SNR regions, such as near the Southeast Indian Ridge and over the abyssal plain between 0°E and 40°E. There are several implications arising from this analysis, which will be discussed in the next section.

## 5. Implications for the Study of the Southern Ocean

The interpretation of jet positions differs substantially between methodologies. Both the PDF method and the WHOSE method give evidence of complex, transient, discontinuous jets that can, particularly in regions away from strong topographic steering (for example, between 0°E and 20°E) form complex, braided jet fields. Additionally, the WHOSE method produces jet fields that contain more fine-scale features in comparison to the other two methods. The differences between methods can be seen most clearly in high eddy kinetic energy regions downstream of large topographic features. In contrast, the contour method presents jets as spatially continuous features that meander with time. While on the broad scale, these two “views” of the ACC converge, the interpretation of an identified jet field may have implications for the study of the regional dynamics of the Southern Ocean.

One particular example of potential implications arising from this work is for the study of the mixing of tracers. It is known that mixing rates in the Southern Ocean are generally higher in so-called “storm tracks” or “hot spots”; regions with strong eddy fields [Thompson and Sallée, 2012]. Shuckburgh et al. [2009] demonstrated that tracer diffusivity results from complicated interactions between strong mean flows and the eddy field, and that mixing is strongest where jets were offset from regions of high eddy activity. The WHOSE method, which can effectively identify jets in low SNR regions, could be a valuable tool for the study of mixing in “hot spot” regions. In contrast, the jet positions indicated by the contour methods do not always correspond to high SSH gradients. Hence, using a definition of a jet from the contour method, calculations of the cross-jet tracer flux may indicate spurious “leakiness,” as the location of the SSH contour may not coincide with strong transport barriers.

It is also important to note that the fine-scale jet field revealed by the WHOSE method reflects the definition of jets as a “local” feature. All the information required to detect the jet is obtained in the immediate neighborhood of the jet. In contrast, the PDF and contour methods define jets from fitting procedures that require information from large geographical region. The advantage of the more “global” definition is that jet filaments separated by large distances can be linked together, even if there is no continuous band of high SSH gradients between them. Additionally, the contour and PDF methods allow jets to be linked to hydrographic fronts and to easily identify the water mass properties of a region [Sokolov and Rintoul, 2002, 2007].

Gradient thresholding and the WHOSE methods lend themselves well to studies where “jets” are interpreted as dynamic jets: strong geostrophic currents that act as transport barriers. The WHOSE method, in particular, can be used to identify mixing barriers in regions of enhanced eddy activity or in high-resolution simulations. For the study of these features, or for the study of the meridional flux of tracers, use of gradient thresholding or the WHOSE method is recommended.

For studies where the regional hydrographic properties are important, the contour method offers several advantages over gradient thresholding and the WHOSE method. The contour method offers a link between the dynamic jets and the hydrographic fronts. The contour method also allows for a more global definition of jet-like features: two jets in different geographical regions can be associated with the same hydrographic front. Studies assessing the transport or trajectories of water masses by the ACC might benefit from the application of the contour method.

The PDF method retains several advantages of the contour method, while allowing a more spatially and temporally varying definition of the particular contour values. For example, downstream of large topographic features where mixing processes are strong one can observe a particular jet shift in SSH space, changing its associated SSH from one value to another [Thompson *et al.*, 2010]. The PDF method also reveals jet fields more reminiscent of those revealed by gradient thresholding or the WHOSE method, with braided, interleaved jets being identified in the OFES data. The PDF method can be considered a kind of “hybrid” method, having some of the advantages of a more local definition of jets, while retaining the ability of contour method to link those jets to hydrographic features. In studies of water mass transformations and jet transitions outside of low SNR regions, the PDF method may provide significant advantages over the others tested here.

## 6. Discussion and Conclusions

### 6.1. Summary

Jets—long, narrow, quasi-zonal currents—form an integral part of the flow of the Southern Ocean, making up the bulk of the flow of the Antarctic Circumpolar Current. They are closely related to hydrographic fronts, which have been subject of numerous studies [Orsi *et al.*, 1995; Belkin and Gordon, 1996]. However, jets are difficult to detect in oceanic data sets due to the influence of noise, eddies and the fact that a universally accepted definition of “jet” does not exist.

A number of jet detection methodologies have been proposed by numerous authors. As jets can be thought of as strong geostrophic currents, they are associated with local maxima in either sea-surface height or sea-surface temperature gradients [Hughes and Ash, 2001; Graham *et al.*, 2012]. However, detecting jets using this gradient thresholding technique has numerous disadvantages, primarily due to the noise amplification and resolution reduction that occurs with the mathematical operation of differentiation. An alternative method for identifying jets, known primarily as the contour method, has been used in a number of studies [Sokolov and Rintoul, 2007; Sallée *et al.*, 2008; Sokolov and Rintoul, 2009a; Langlais *et al.*, 2011; Volkov and Zlotnicki, 2012]. Sokolov and Rintoul [2007] found that strong SSH gradients are frequently found aligned with a particular SSH contour. By tracking that contour in time and space, one can track the jet. However Thompson *et al.* [2010] and Graham *et al.* [2012] have found several weaknesses with contour methods, in particular noting that the SSH value associated with a jet can change in both space and time. Although Graham *et al.* [2012] suggest that gradient thresholding methods have some advantages over contour methods, their limitations restrict their use in high-resolution data sets. A recent study by Thompson *et al.* [2010] developed a novel jet detection method based on probability density functions which avoids several of the limitation of both gradient thresholding and contour methods. This method has not been subject to rigorous testing and comparison with other methods.

In this paper, we have sought to accomplish two objectives: address some of the shortcomings associated with gradient thresholding techniques and to undertake a systematic comparison of several commonly used jet detection methods, both quantitatively and qualitatively.

In order to improve the gradient thresholding techniques, we take inspiration from methods found in signal processing for the detection of steps and pulses in noisy data. This new method is based on the approach of Ravier and Amblard [2001], which combines wavelet analysis, an effective technique for determining the

"scales" present in a signal, and higher order statistics (HOS) which can be used to separate step-like signals from noise [Lacoume *et al.*, 1997]. This method improves the problems of noise amplification that occur in a naïve implementation of gradient thresholding.

Our new Wavelet/HOS Enhancement (WHOSE) method is compared with the standard gradient thresholding, the PDF method of Thompson *et al.* [2010] and the contour method of Sokolov and Rintoul [2007] using synthetically generated SSH fields. The "mean" field consists of a single jet, taken to be a step in the SSH, while the "eddy" field was generated as a 2-D field of colored noise, with the spectrum taken from the altimetric observations of Xu and Fu [2011]. These synthetic data allow us to quantitatively compare the accuracy of each method as the location of the jet can be set a priori. Using a Monte-Carlo approach, we find that WHOSE method performs well at a broad range of signal-to-noise ratios. When compared to the simple gradient thresholding described in Graham *et al.* [2012] and the PDF method of Thompson *et al.* [2010], we find that the WHOSE method is able to detect jets at lower signal-to-noise ratios (SNR) and has superior accuracy at a higher SNR. However, the contour method is found to have superior accuracy when applied to the synthetic SSH fields. We note that the synthetic jets used here are particularly responsive to analysis by the contour method, as the jet core lies on a single SSH contour by construction. All methods show a decrease in accuracy as the SNR decreases, with the WHOSE and contour methods having a slower reduction in accuracy than the other methods tested here.

We performed a detailed comparison of the WHOSE, PDF, and contour methods using the output of a high-resolution simulation of the Southern Ocean. We have chosen to use the simulation from the OFES model [Masumoto *et al.*, 2004], since it has been shown accurately represent the jets and eddies that make up the Antarctic Circumpolar Current system. In regions where flow is strongly steered by topography (for example, the Kerguelen and Campbell Plateaus) there is consensus amongst the methods, each showing strongly steered jets with reduced variability. There is also strong consensus amongst the methods regarding the regions where jets exhibit strong time variability and where jets are more time invariant. Each of the methods under consideration gives a similar "big picture" view of the Antarctic Circumpolar Current. In the future, combining these methods with careful estimates of the SSH gradient, perhaps employing the WHOSE denoising procedures, or with existing methods, such as those of Gille [1994] could enable improved estimation of the amplitudes of steps in the SSH field, and consequently, the along-jet velocity.

Finally, we discuss the implications of our work for the study of the Southern Ocean. The flow field of the Southern Ocean is complicated, and the nature of the jet field within the ACC is dependent on the methods used to analyze it. The gradient thresholding and WHOSE methods, which effectively detect regions of high SSH gradients, are "local" methods: jets are defined using only information found in the immediate vicinity of the jet itself. In contrast, the contour method fits SSH contours to regions of high SSH gradients over a large area. Contour methods are "global" methods: information from a broad geographical region is taken into account when identifying a jet at a particular location. Contour methods are useful for linking together jet features separated by large distances, while the WHOSE and gradient thresholding methods are useful for identifying local transport barriers and strong currents. The PDF method represents a hybrid of "global" and "local" methods.

In this paper, we have demonstrated that how one interprets the flow in this important region is dependent on the methods chosen to analyze it. In their study, Langlais *et al.* [2011] concluded that "There is, in fact, no single answer to the question of 'how many fronts does the ACC contain?'" The conclusions of this study are similar: there is no "correct" method for analyzing jets and fronts in the Southern Ocean. The choice of method should always be motivated by the purpose of the study and the data at hand.

The WHOSE method retains many of the advantages of standard gradient thresholding method. The method is quasi objective: the user specifies the input parameters: the cutoff wave number of along-jet smoothing,  $k_{\text{cutoff}}$ , the confidence parameter for the Bienaymé–Chebyshev inequality,  $\alpha$ , and the threshold for the final jet detection. Once specified, the detector objectively identifies jets. There is no a priori determination of, say, the number of jets that will be detected, or their persistence. This is contrast to methods such as Sokolov and Rintoul [2007] where some input parameter implicitly selects the number of jets to be detected (in the case of Sokolov and Rintoul [2007], the fraction of total sea surface area covered by regions where the gradient of sea-surface height exceeds some threshold), or methods such as Langlais *et al.* [2011] where fronts are a priori specified to exist on certain isotherms.

Despite these advantages, the WHOSE method also has several disadvantages when compared with other methods. In comparison to the PDF method, the WHOSE method has a number of parameters that need to be selected by the user. Experimentation has found that the results of the WHOSE method are not particularly sensitive to variations in zonal smoothing parameter  $k_{\text{cutoff}}$  or the confidence parameter  $\alpha$ , but are quite sensitive to changes in final thresholding parameter. In particular, we have found that the rate of false positive detection is sensitive to the value of the threshold selected: as such, this threshold must be selected carefully in order to eliminate false positive detection while still detecting the real jet cores. This procedure is both subjective and requires trial-and-error by the user. This is a weakness of many jet detection methods and that our eddy and noise suppression steps can help refine the guess of the gradient threshold by improving the SNR.

### Acknowledgments

The OFES simulation was conducted on the Earth Simulator under the support of JAMSTEC. OFES data are available at <http://www.jamstec.go.jp/esc/research/AtmOcn/product/ofes.html>. The ETOPO data set is provided by the NOAA National Geophysical Data Center. ETOPO data are available at [www.ngdc.noaa.gov/mgg/global/global.html](http://www.ngdc.noaa.gov/mgg/global/global.html). The author wishes to acknowledge helpful conversations with A. Mc. Hogg and S. R. Rintoul and comments on the draft manuscript by A. Klocker. The author was supported by a CSIRO Wealth from Oceans flagship scholarship.

### References

- Alyt, O. A. M., A. S. Omar, and A. Z. Elsherbeni (2006), Detection and localization of rf radar pulses in noise environments using wavelet packet transform and higher order statistics, *Prog. Electromagn. Res.*, 58, 301–317, doi:10.2528/PIER05070204.
- Amante, C., and B. W. Eakins (2009), Etopo1 1 arc-minute global relief model: Procedures, data sources and analysis, *NOAA Tech. Memo. NESDIS NGDC-24*, National Oceanic and Atmospheric Administration, Boulder, Colo.
- Arbic, B. K., R. B. Scott, D. B. Chelton, J. G. Richman, and J. F. Shriver (2012), Effects of stencil width on surface ocean geostrophic velocity and vorticity estimation from gridded satellite altimeter data, *J. Geophys. Res.*, 117, C03029, doi:10.1029/2011JC007367.
- Belkin, I. M., and A. L. Gordon (1996), Southern ocean fronts from the greenwich meridian to tasmania, *J. Geophys. Res.*, 101(C2), 3675–3696, doi:10.1029/95JC02750.
- Billany, W., S. Swart, J. Hermes, and C. Reason (2010), Variability of the southern ocean fronts at the greenwich meridian, *J. Mar. Syst.*, 82(4), 304–310, doi:10.1016/j.jmarsys.2010.06.005.
- Burls, N. J., and C. J. C. Reason (2006), Sea surface temperature fronts in the midlatitude south atlantic revealed by using microwave satellite data, *J. Geophys. Res.*, 111, C03029, doi:10.1029/2005JC003133.
- Carter, B. C., M. Vershinin, and S. P. Gross (2008), A comparison of step-detection methods: How well can you do?, *Biophys. J.*, 94(1), 306–319.
- De Boer, A. M., R. M. Graham, M. D. Thomas, and K. E. Kohfeld (2013), The control of the southern hemisphere westerlies on the position of the subtropical front, *J. Geophys. Res. Oceans*, 118, 5669–5675, doi:10.1002/jgrc.20407.
- Doglioli, A. M., B. Blanke, S. Speich, and G. Lapeyre (2007), Tracking coherent structures in a regional ocean model with wavelet analysis: Application to cape basin eddies, *J. Geophys. Res.*, 112, C05043, doi:10.1029/2006JC003952.
- Dong, S., J. Sprintall, and S. T. Gille (2006), Location of the antarctic polar front from amsr-e satellite sea surface temperature measurements, *J. Phys. Oceanogr.*, 36(11), 2075–2089, doi:10.1175/JPO2973.1.
- Donoho, D. L., and J. M. Johnstone (1994), Ideal spatial adaptation by wavelet shrinkage, *Biometrika*, 81(3), 425–455, doi:10.1093/biomet/81.3.425.
- Dritschel, D. G., and M. E. McIntyre (2008), Multiple jets as PV staircases: The Phillips effect and the resilience of eddy-transport barriers, *J. Atmos. Sci.*, 65(3), 855–874.
- Farge, M. (1992), Wavelet transforms and their applications to turbulence, *Annu. Rev. Fluid Mech.*, 24(1), 395–458, doi:10.1146/annurev.fl.24.010192.002143.
- Ferrari, R., and M. Nikurashin (2010), Suppression of eddy diffusivity across jets in the southern ocean, *J. Phys. Oceanogr.*, 40(7), 1501–1519.
- Fowler, J. (2005), The redundant discrete wavelet transform and additive noise, *IEEE Signal Process. Lett.*, 12(9), 629–632, doi:10.1109/LSP.2005.853048.
- Gille, S. T. (1994), Mean sea surface height of the Antarctic circumpolar current from geosat data: Method and application, *J. Geophys. Res.*, 99(C9), 18,255–18,273, doi:10.1029/94JC01172.
- Graham, R. M., and A. M. De Boer (2013), The dynamical subtropical front, *J. Geophys. Res. Oceans*, 118, 5676–5685, doi:10.1002/jgrc.20408.
- Graham, R. M., A. M. de Boer, K. J. Heywood, M. Chapman, and D. P. Stevens (2012), Southern ocean fronts: Controlled by wind or topography?, *J. Geophys. Res.*, 117, C08018, doi:10.1029/2012JC007887.
- Hallberg, R., and A. Gnanadesikan (2006), The role of eddies in determining the structure and response of the wind-driven southern hemisphere overturning: Results from the modeling eddies in the southern ocean (meso) project, *J. Phys. Oceanogr.*, 36(12), 2232–2252.
- Hughes, C. W., and E. R. Ash (2001), Eddy forcing of the mean flow in the Southern Ocean, *J. Geophys. Res.*, 106(C2), 2713–2722, doi:10.1029/2000JC00332.
- Hughes, C. W., A. F. Thompson, and C. Wilson (2010), Identification of jets and mixing barriers from sea level and vorticity measurements using simple statistics, *Ocean Modell.*, 32(1–2), 44–57, doi:10.1016/j.ocemod.2009.10.004.
- Ivchenko, V. O., S. Danilov, and D. Olbers (2013), *Eddies in Numerical Models of the Southern Ocean*, pp. 177–198, AGU, Washington, D. C., doi:10.1029/177GM13.
- Kaspi, Y., and G. R. Flierl (2007), Formation of jets by baroclinic instability on gas planet atmospheres, *J. Atmos. Sci.*, 64(9), 3177–3194, doi:10.1175/JAS4009.1.
- Klocker, A., R. Ferrari, and J. H. LaCasce (2012), Estimating suppression of eddy mixing by mean flows, *J. Phys. Oceanogr.*, 42(9), 1566–1576, doi:10.1175/JPO-D-11-0205.1.
- Kostianoy, A. G., A. I. Ginzburg, M. Frankignoulle, and B. Delille (2004), Fronts in the southern Indian ocean as inferred from satellite sea surface temperature data, *J. Mar. Syst.*, 45(1–2), 55–73, doi:10.1016/j.jmarsys.2003.09.004.
- Lacoume, J.-L., P.-O. Amblard, and P. Comon (1997), Statistiques d'ordres supérieurs pour le traitement du signal, *Collect. Sci. de l'Ingenieur*, Masson, Paris, France.
- Langlais, C., S. Rintoul, and A. Schiller (2011), Variability and mesoscale activity of the southern ocean fronts: Identification of a circumpolar coordinate system, *Ocean Modell.*, 39(1–2), 79–96, doi:10.1016/j.ocemod.2011.04.010.
- Luo, J., and L. Jameson (2002), A wavelet-based technique for identifying, labeling, and tracking of ocean eddies, *J. Atmos. Oceanic Technol.*, 19(3), 381–390.
- Mallat, S., and S. Zhong (1992), Characterization of signals from multiscale edges, *IEEE Trans. Pattern Anal. Mach. Intell.*, 14(7), 710–732, doi:10.1109/34.142909.

- Marshall, J., D. Olbers, H. Ross, and D. Wolf-Gladrow (1993), Potential vorticity constraints on the dynamics and hydrography of the southern ocean, *J. Phys. Oceanogr.*, 23(3), 465–487.
- Masumoto, Y., et al. (2004), A fifty-year eddy-resolving simulation of the world ocean, *J. Earth Simulator*, 1, 35–56.
- Mendel, J. (1991), Tutorial on higher-order statistics (spectra) in signal processing and system theory: Theoretical results and some applications, *Proc. IEEE*, 79(3), 278–305, doi:10.1109/5.75086.
- Moore, J. K., M. R. Abbott, and J. G. Richman (1999), Location and dynamics of the antarctic polar front from satellite sea surface temperature data, *J. Geophys. Res.*, 104(C2), 3059–3073, doi:10.1029/1998JC900032.
- Morrow, R., and P.-Y. Le Traon (2012), Recent advances in observing mesoscale ocean dynamics with satellite altimetry, *Adv. Space Res.*, 50(8), 1062–1076, doi:10.1016/j.asr.2011.09.033.
- Nadernejad, E., S. Sharifzadeh, and H. Hassanpour (2008), Edge detection techniques: Evaluations and comparison, *Appl. Math. Sci.*, 2(31), 1507–1520.
- Orsi, A. H., T. I. Whitworth, and W. D. J. Nowlin (1995), On the meridional extent and fronts of the Antarctic Circumpolar Current, *Deep Sea Res., Part I*, 42(5), 641–673, doi:10.1016/0967-0637(95)00021-W.
- Park, Y.-H., F. Roquet, I. Durand, and J.-L. Fuda (2008), Large-scale circulation over and around the northern kerguelen plateau, *Deep Sea Res., Part II*, 55(5–7), 566–581, doi:10.1016/j.dsr2.2007.12.030.
- Percival, D. (2008), Analysis of geophysical time series using discrete wavelet transforms: An overview, in *Nonlinear Time Series Analysis in the Geosciences, Lecture Notes in Earth Sciences*, vol. 112, edited by R. Donner and S. Barbosa, pp. 61–79, Springer, Berlin, Germany. doi:10.1007/978-3-540-78938-3\_4.
- Ravier, P., and P.-O. Amblard (1998), Combining an adapted wavelet analysis with fourth-order statistics for transient detection, *Signal Process.*, 70(2), 115–128, doi:10.1016/S0165-1684(98)00117-0.
- Ravier, P., and P.-O. Amblard (2001), Wavelet packets and de-noising based on higher-order-statistics for transient detection, *Signal Process.*, 81(9), 1909–1926, doi:10.1016/S0165-1684(01)00088-3.
- Rhines, P. B. (1994), Jets, *Chaos*, 4(2), 313–339, doi:10.1063/1.166011.
- Roquet, F. (2009), La circulation océanique autour du plateau de kerguelen de l'observation à la modélisation, PhD thesis, L'Université Paris VI, Paris, France.
- Sadler, B., and A. Swami (1999), Analysis of multiscale products for step detection and estimation, *IEEE Trans. Inf. Theory*, 45(3), 1043–1051, doi:10.1109/18.761341.
- Sallée, J. B., K. Speer, and R. Morrow (2008), Response of the antarctic circumpolar current to atmospheric variability, *J. Clim.*, 21(12), 3020–3039.
- Shuckburgh, E., H. Jones, J. Marshall, and C. Hill (2009), Understanding the regional variability of eddy diffusivity in the Pacific sector of the Southern Ocean, *J. Phys. Oceanogr.*, 39(9), 2011–2023, doi:10.1175/2009JPO4115.1.
- Siegel, A., and J. B. Weiss (1997), A wavelet-packet census algorithm for calculating vortex statistics, *Phys. Fluids*, 9(7), 1988–1999, doi:10.1063/1.869318.
- Smith, S. (2003), *Digital Signal Processing: A Practical Guide for Engineers and Scientists*, Newnes, Burlington, Mass.
- Sokolov, S., and S. R. Rintoul (2002), Structure of southern ocean fronts at 140°E, *J. Mar. Syst.*, 37(1-3), 151–184, doi:10.1016/S0924-7963(02)00200-2.
- Sokolov, S., and S. R. Rintoul (2007), multiple jets of the Antarctic Circumpolar Current south of Australia\*, *J. Phys. Oceanogr.*, 37(5), 1394–1412.
- Sokolov, S., and S. R. Rintoul (2009a), Circumpolar structure and distribution of the Antarctic circumpolar current fronts: 2. Variability and relationship to sea surface height, *J. Geophys. Res.*, 114, C11019, doi:10.1029/2008JC005248.
- Sokolov, S., and S. R. Rintoul (2009b), Circumpolar structure and distribution of the Antarctic circumpolar current fronts: 1. Mean circumpolar paths, *J. Geophys. Res.*, 114, C11018, doi:10.1029/2008JC005108.
- Taswell, C. (2000), The what, how, and why of wavelet shrinkage de-noising, *Comput. Sci. Eng.*, 2(3), 12–19, doi:10.1109/5992.841791.
- Thompson, A. (2008), The atmospheric ocean: Eddies and jets in the Antarctic Circumpolar Current, *Philos. Trans. R. Soc. A*, 366, 4529–4541, doi:10.1098/rsta.2008.0196.
- Thompson, A. F. (2010), Jet formation and evolution in baroclinic turbulence with simple topography, *J. Phys. Oceanogr.*, 40(2), 257–278.
- Thompson, A. F., and K. J. Richards (2011), Low frequency variability of southern ocean jets, *J. Geophys. Res.*, 116, C09022, doi:10.1029/2010JC006749.
- Thompson, A. F., and J.-B. Sallée (2012), Jets and topography: Jet transitions and the impact on transport in the Antarctic circumpolar current, *J. Phys. Oceanogr.*, 42(6), 956–972.
- Thompson, A. F., P. H. Haynes, C. Wilson, and K. J. Richards (2010), Rapid southern ocean front transitions in an eddy-resolving ocean GCM, *Geophys. Res. Lett.*, 37, L23602, doi:10.1029/2010GL045386.
- Volkov, D. L., and V. Zlotnicki (2012), Performance of GOCE and GRACE-derived mean dynamic topographies in resolving Antarctic Circumpolar Current fronts, *Ocean Dyn.*, 62(6), 893–905, doi:10.1007/s10236-012-0541-9.
- Williams, R. G., C. Wilson, and C. W. Hughes (2007), Ocean and atmosphere storm tracks: The role of eddy vorticity forcing, *J. Phys. Oceanogr.*, 37(9), 2267–2289.
- Wu, J.-J. (2000), Simulation of rough surfaces with fft, *Tribology Int.*, 33(1), 47–58, doi:10.1016/S0301-679X(00)00016-5.
- Xu, Y., and L.-L. Fu (2011), Global variability of the wavenumber spectrum of oceanic mesoscale turbulence, *J. Phys. Oceanogr.*, 41(4), 802–809.